Journal of Computational and Applied Mathematics 313 (2017) 454–468

Contents lists available at ScienceDirect

Journal of Computational and Applied Mathematics

journal homepage: www.elsevier.com/locate/cam

An isogeometric boundary element method for three dimensional potential problems

Y.P. Gong, C.Y. Dong *, X.C. Qin

Department of Mechanics, School of Aerospace Engineering, Beijing Institute of Technology, Beijing 100081, China

ARTICLE INFO

Article history:
Received 16 June 2016
Received in revised form 5 October 2016

Keywords:
Potential problems
3D IGABEM
Singular integrals
Power series expansion method

ABSTRACT

Isogeometric analysis (IGA) coupled with boundary element method, i.e. IGABEM, received a lot of attention in recent years. In this paper, we extend the IGABEM to solve 3D potential problems. This method offers a number of key improvements compared with conventional piecewise polynomial formulations. Firstly, the models for analysis in the IGABEM are exact geometrical representation no matter how coarse the discretization of the studied bodies is, thus the IGABEM ensures that no geometrical errors are produced in the analysis process. Secondly, a meshing process is no longer required, which means redundant computations are eliminated to allow analysis to be carried out with greatly reduced pre-processing. To accurately evaluate the singular integrals appearing in our method, the power series expansion method is employed. The integration surface is on the real surface of the model, rather than the interpolation surface, i.e. no geometrical errors. Thus, the value of integral is more accurate than the traditional boundary element method, which can improve the computation accuracy of the IGABEM. Some numerical examples for 3D potential problems are used to validate the solutions of the present method with analytical and numerical solutions available.

1. Introduction

Isogeometric analysis (IGA), established by Hughes et al. [1], is a new numerical method that has received a lot of attention over the last ten years. The central idea of the method is to bridge the gap between computer aided design (CAD) and finite element analysis (FEA) by applying basis functions that are typically used in computer aided design (CAD) to the analysis, instead of the conventional polynomial basis functions. The main benefit of isogeometric method is that the geometry of the problem is preserved exactly. When building the models using CAD software, we can directly carry out numerical analysis based on the isogeometric method, i.e. there is no transformation from the CAD models to the computational meshes. In addition, in the implementation of the IGA the mesh refinement can be highly simplified using the standard knot-insertion and/or degree-elevation procedures [2] without communicating with the CAD system, once the initial mesh is completed.

The IGA was originally presented to focus on the use of the finite element method (FEM), but many researchers also applied the IGA to the boundary element method (BEM) where distinct advantages such as reduction of problem dimensionality by one are found. The IGA coupled with the BEM, i.e. IGABEM, has achieved rapid development recently [3–5] and has been successfully applied to investigate various problems, e.g. elasticity problems [6,7], potential problems [8], Laplace equation [9], fast multipole IGABEM [10,11], Helmholtz problems [12], ship wave-resistance problem [13,14], acoustic problems [15,16], shape optimization [17–19], nonsingular IGABEM analysis [20], weakly-singular integral equation [21], crack problem [22] and adaptive mesh-refinement [23].

* Corresponding author.
E-mail address: cydong@bit.edu.cn (C.Y. Dong).

http://dx.doi.org/10.1016/j.cam.2016.10.003
0377-0427/

Compared with traditional BEM, the models for analysis in the IGABEM are exact geometrical representation no matter how coarse the discretization of the studied bodies is, thus the IGABEM ensures that no geometrical errors appear in the analysis process. This is a distinct advantage over traditional BEM, in which the geometrical errors will greatly influence the accuracy of the numerical result, especially for complex models or thin-body/coating structures. In addition, as we have known that in the implementation of the IGAFEM the information of the domains is needed which is still a challenging problem. However, the IGABEM only requires a boundary description of the problem which creates a perfect match with the CAD, since the output of such software is only a boundary discretization. Moreover, when the IGABEM is used to shape design optimization problems, it can provide more accurate sensitivity of complicated geometries including higher order effects such as curvature, normal and tangential vectors. Because the NURBS functions of higher continuity offer a much more compact representation of response and sensitivity of structures than the standard basis functions do, so it can yield better accuracy even at the same polynomial order.

However, the IGABEM formulation contains varied orders of singular integrals, which requires careful study and analysis. Up to now, tremendous effort has been devoted to deriving convenient integral forms or sophisticated computational techniques to eliminate the singularities appearing in boundary integral equations. These methods can be summarized on the whole as two categories: the local and the global strategies. The local strategies are employed to calculate the singular integrals directly. They usually include but are not limited to, analytical and semi-analytical methods [24,25], new Gaussian quadrature approach [26], the local regularization method [27,28], transformation method [29–31], finite-part integral method [32,33], subtraction technique [34,35], etc. Among these methods, the local regularization technique proposed by Guiggiani et al. [36,37] was extensively employed to remove various orders of singularities. Although the method was successfully used to evaluate the strong singular integral appearing in 2D IGABEM [5,6], it requires the expansion of all quantities of the integrand into Taylor's series, which may be arduous and computationally expensive [38,39]. The power series expansion method presented by Gao [40] seems to be a more accurate and flexible method for evaluating 2D or 3D singular boundary integrals by expressing the non-singular part of a singular integrand as well as the global distance r as power series in the local distance ρ of the intrinsic coordinate system.

In this paper, the power series expansion method [40] is used to compute the singular integrals appearing in the 3D IGABEM. Firstly, the singular surface integral is divided into a line integral over the contour of the integration surface and a radial integral containing the singularities by the radial integration method (RIM) [41,42]. Then the singularities condensed in the radial integral are removed analytically or numerically by extracting the finite value parts from the power series expansions. Finally, the line integral with regular kernel functions can be computed by the standard Gaussian quadrature. Through the above procedure, singular integrals over isogeometric boundary elements can be evaluated with high accuracy, even when the order of singularity is high. One of the features of the method is that integration surface is on the real surface of the model rather than the interpolation surface, i.e. no geometrical errors. Thus, the value of integral is more accurate than the traditional boundary element method [40].

A brief outline of this paper is as follows. A short introduction to B-spline and NURBS is given in Section 2. In Section 3, the numerical implementation of the IGABEM for 3D potential problems is performed. Several numerical examples are given in Section 4 to verify the efficiency and accuracy of the present method. Finally, we present the conclusions for our work.

2. B-splines and NURBS

In this work, we focus our attention on the numerical implementation of the IGABEM for 3D potential problems. Thus only some conclusions are given, more details about the IGABEM can be found in [1,5,6,43].

2.1. B-spline and NURBS basis functions

B-spline basis functions of degree p are defined recursively with piecewise constants ($p = 0$)

$$N_{i,0} = \begin{cases} 1 & \text{if } \xi_i \le \xi < \xi_{i+1}, \\ 0 & \text{otherwise} \end{cases} \tag{1}$$

where $1 \le i \le n$, n is the number of basis functions which form the B-spline. For $p = 1, 2, 3, \ldots$, they are defined by

$$N_{i,p}(\xi) = N_{i,p-1}(\xi)\,(\xi - \xi_i) \,/\, \left(\xi_{i+p} - \xi_i\right) + N_{i+1,p-1}(\xi)\,\left(\xi_{i+p+1} - \xi\right) \,/\, \left(\xi_{i+p+1} - \xi_{i+1}\right). \tag{2}$$

The B-spline can be considered as a sub-set of NURBS. NURBS basis functions are defined as

$$R_{i,p}(\xi) = N_{i,p}(\xi)\omega_i \Big/ \left(\sum_{j=1}^{n} N_{j,p}(\xi)\omega_j\right) \tag{3}$$

where $N_{i,p}$ is the ith B-spline basis function of order p. ω_i is the ith positive weight. The values of ω_i depend on the type and shape of curves.

To define a B-spline or NURBS curve several other items are required [1,5,6,43], such as curve degree$p$, control points $\boldsymbol{P}$, knot vector $\mathbf{U}$.

2.2. B-spline and NURBS surfaces

Given a control net $\{P_{i,j}\},\ i = 1, 2, \ldots, n,\ j = 1, 2, \ldots, m$, and two knot vectors (one for each parametric direction) $\mathbf{U} = \{\xi_1, \xi_2, \ldots, \xi_{n+p+1}\}$ and $\mathbf{V} = \{\eta_1, \eta_2, \ldots, \eta_{m+q+1}\}$, a tensor product B-spline surface is defined by

$$S(\xi, \eta) = \sum_{i=1}^{n}\sum_{j=1}^{m} N_{i,j}^{p,q}(\xi, \eta)P_{i,j} \tag{4}$$

where $N_{i,j}^{p,q}(\xi, \eta) = N_{i,p}(\xi)M_{j,q}(\eta)$, m (n) is the number of basis functions in the parametric direction $\eta(\xi)$. $N_{i,p}(\xi)$ and $M_{j,q}(\eta)$ are the univariate B-spline basis functions of orders p and q corresponding to knot vectors $\mathbf{U}$ and $\mathbf{V}$, respectively.

Similar to B-spline surfaces, a tensor-product NURBS surface is defined as

$$S(\xi, \eta) = \sum_{i=1}^{n}\sum_{j=1}^{m} R_{i,j}^{p,q}P_{i,j} \tag{5}$$

where the bivariate basis functions $R_{i,j}^{p,q}$ are given by

$$R_{i,j}^{p,q}(\xi, \eta) = \left(N_i(\xi)M_j(\eta)\omega_{i,j}\right) \Bigg/ \left(\sum_{\hat{i}=1}^{n}\sum_{\hat{j}=1}^{m} N_{\hat{i}}(\xi)M_{\hat{j}}(\eta)\omega_{\hat{i},\hat{j}}\right). \tag{6}$$

In our work, the isogeometric analysis relies on the use of the bivariate NURBS basis functions given above. We use the NURBS basis functions to describe the geometry of the problem and approximate the unknown fields in the governing PDEs.

3. Implementation of isogeometric analysis in BIEs

3.1. Boundary integral equation

Considering the boundary integral equation of 3D potential problems in the domain Ω enclosed by boundary Γ, the usual direct BEM formulation is presented as follows [44–47]:

$$c(\mathbf{y})u(\mathbf{y}) = \int_{\Gamma} q(\mathbf{x})u^*(\mathbf{x}, \mathbf{y})d\Gamma(\mathbf{x}) - \int_{\Gamma} u(\mathbf{x})q^*(\mathbf{x}, \mathbf{y})d\Gamma(\mathbf{x}) \tag{7}$$

where $\mathbf{y}$ and $\mathbf{x}$ are the source and the field points, respectively. c is a coefficient depending on the smoothness of the boundary at the source point $\mathbf{y}$.$u^*(\mathbf{x}, \mathbf{y})$ represents the fundamental solution and $q^*(\mathbf{x}, \mathbf{y})$ is its normal derivative.

3.2. Isogeometric approximation

Different from conventional BEM, the basis function of the IGABEM is chosen to exactly capture the geometry. In the implementation of 3D IGABEM, we use two knot vectors $\mathbf{U}$ and $\mathbf{V}$, $m \times n$ control points $\{P_{i,j}\},\ i = 1, 2, \ldots, n,\ j = 1, 2, \ldots, m$, and curve orders p and q to build the boundary shape and the basis functions. As is shown in Fig. 1 elements of the integral boundary are defined in the parametric space as non-zero knots span $[\xi_i,\ \xi_{i+1}] \times \left[\eta_j,\ \eta_{j+1}\right]$, where $\xi_i,\ \xi_{i+1} \in \mathbf{U}$ and $\eta_j,\ \eta_{j+1} \in \mathbf{V}$.

In order to carry out the numerical integration using Gauss–Legendre quadrature, local coordinates $\bar{\xi}$ and $\bar{\eta}$ must be in the range $[-1, 1]\times[-1, 1]$. Therefore, there should be a transformation from the parameter space $(\xi, \eta) \in [\xi_i,\ \xi_{i+1}]\times\left[\eta_j,\ \eta_{j+1}\right]$ (ξ_i is the ith knot in $\mathbf{U}$ and η_j is the jth knot in $\mathbf{V}$, i and j are respectively the knot indexes in directions ξ and η) to the Gauss–Legendre range $[-1, 1] \times [-1, 1]$. Fig. 1 gives some illustration for physical domain Ω, parametric domain $\hat{\Omega}$ and parent element.

To approximate the geometry and unknown fields, the non-zero basis functions must be determined for a particular element. After this is done, a set of local basis functions that are related to the global basis functions is given as

$$N_b^e(\bar{\xi}, \bar{\eta}) \equiv R_a^{p,q}(\xi(\bar{\xi}), \eta(\bar{\eta})) \tag{8}$$

where the local basis function number b, element number e and global basis function number are related by $a = \mathrm{conn}(e, b)$, where conn() is a connectivity function. Up to now, the geometry, potential and flux can be easily interpolated by Eq. (5) as

$$\mathbf{x}_e(\xi, \eta) = \sum_{b=1}^{(p+1)(q+1)} R_{i,j}^{p,q}(\xi, \eta)\,\mathbf{x}_b;\ u_e(\xi, \eta) = \sum_{b=1}^{(p+1)(q+1)} R_{i,j}^{p,q}(\xi, \eta)\,d_b;\ q_e(\xi, \eta) = \sum_{b=1}^{(p+1)(q+1)} R_{i,j}^{p,q}(\xi, \eta)\,t_b \tag{9}$$

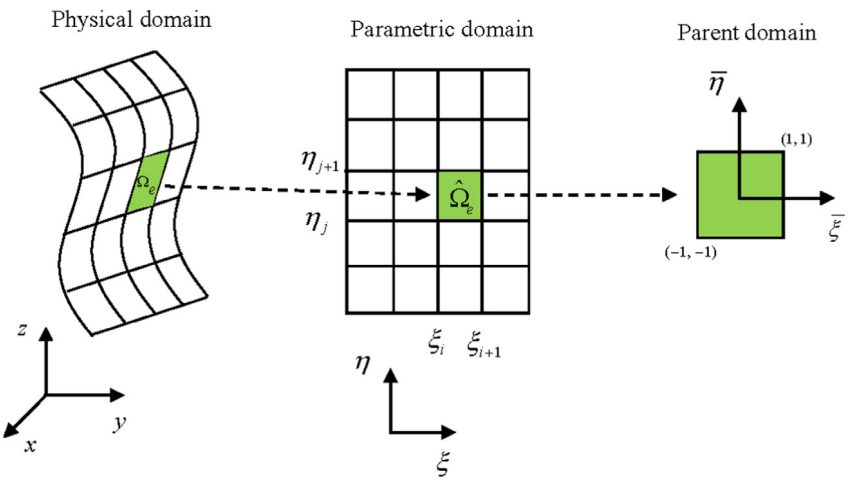

Fig. 1. Definition of domains used for integration in isogeometric analysis.

where $\mathbf{x}_b$, d_b and t_b represent the coordinate, potential and flux coefficients at a particular control point. Thus, we can obtain the 3D isogeometric boundary integral equation as follows

$$C(x')\sum_{l=1}^{(p+1)(q+1)} N_l^{\bar{e}}(\bar{\xi}', \bar{\eta}')u^{le} + \sum_{e=1}^{N_e}\sum_{l=1}^{(p+1)(q+1)}\left[\int_{-1}^{1}\int_{-1}^{1} q^*\left(x', x\left(\bar{\xi}, \bar{\eta}\right)\right) N_l^e(\bar{\xi}, \bar{\eta})J(\bar{\xi}, \bar{\eta})d\bar{\xi}d\bar{\eta}\right] d^{le}$$
$$= \sum_{e=1}^{N_e}\sum_{l=1}^{(p+1)(q+1)}\left[\int_{-1}^{1}\int_{-1}^{1} u^*\left(x', x\left(\bar{\xi}, \bar{\eta}\right)\right) N_l^e(\bar{\xi}, \bar{\eta})J(\bar{\xi}, \bar{\eta})d\bar{\xi}d\bar{\eta}\right] t^{le} \tag{10}$$

where x' represents the collocation point. $\bar{\xi}'$ and $\bar{\eta}'$ represent the local coordinates of the collocation point x' on element $\bar{e}$.

3.3. Collocation point for 3D IGABEM

In the IGABEM, since the control points are usually not being on the boundary, so the normal practice of collocation points at nodal positions for conventional BEM is no longer valid. For 2D IGABEM [6], Simpson et al. used the Greville abscissae definition [48,49] to define the position of collocation points in parameter space. Similarly, we have for 3D IGABEM

$$\begin{aligned} \xi_i' &= \left(\xi_{i+1} + \xi_{i+2} + \cdots + \xi_{i+p}\right)/p \quad i = 1, 2, \ldots, n \\ \eta_j' &= \left(\xi_{j+1} + \xi_{j+2} + \cdots + \xi_{j+q}\right)/q \quad j = 1, 2, \ldots, m \end{aligned} \tag{11}$$

where n and m are the number of control points along ξ and η directions, respectively. p and q are the orders of the curves along ξ and η directions, respectively. Thus, the parameter coordinates of the collocation points can be given as $(\xi_i', \ \eta_j')$. We can easily get the coordinates of the collocation points using the NURBS interpolation (Eq. (5)).

3.4. Integration implementation

In the implementation of BEM, the accurate evaluation of the singular integrals is a crucial and difficult task. Simpson et al. [6] used Subtraction of Singularity Method (SST) and Telles transformation to evaluate strongly and weakly singular integrals appearing in 2D IGABEM, respectively. Here both the strongly and weakly singular integrals in 3D IGABEM are computed by the power series expansion method [40]. In order to eliminate singularities in 3D boundary integrals, the radial integration method (RIM) [41,42] is employed, in which a surface integral is divided into a line integral over contour of the integration surface and a radial integral containing the singularities. The singularities condensed in the radial integral are removed analytically or numerically by extracting the finite value parts from the power series expansion.

3.4.1. Evaluation of 3D singular boundary integrals

As is well-known in BEM, when the source point $\mathbf{x}^P$ is located on the element under integration, the distance r may approach zero so that the singularity appears. Now, consider the 3D boundary integral $I^e(\mathbf{x}^P)$ on element e.

$$I^e(\mathbf{x}^P) = \int_{\Gamma_e} \bar{f}(\mathbf{x}^P, \mathbf{x})/r^\beta(\mathbf{x}^P, \mathbf{x})d\Gamma = \int_{\eta_j}^{\eta_{j+1}}\int_{\xi_i}^{\xi_{i+1}} \bar{f}(\mathbf{x}^P, \mathbf{x})/r^\beta(\mathbf{x}^P, \mathbf{x})d\xi d\eta \tag{12}$$

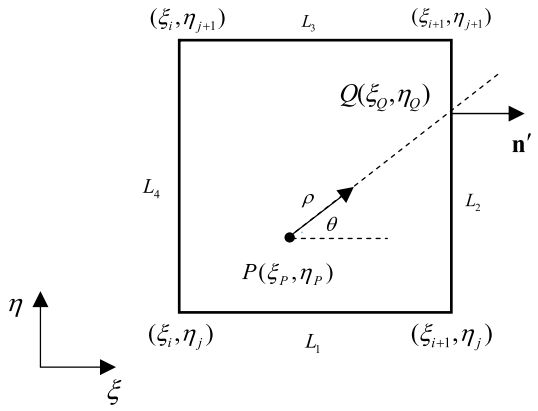

Fig. 2. Integration plane in intrinsic coordinate system.

where β is a constant and $\bar{f}(\mathbf{x}^P, \mathbf{x})$ is bounded everywhere for the variable $\mathbf{x}$. Using the radial integration method (RIM) presented by Gao [41,42], the integral in Eq. (12) can be transformed into a contour ($L = \sum_{i=1}^{4} L_i$) integral along the four sides of the element, i.e.

$$I^e(\mathbf{x}^P) = \int_L F(\mathbf{x}^P, \mathbf{x}^Q)\ \partial\rho(P,Q)/\left(\rho(P,Q)\ \partial\mathbf{n}'\right) dL(Q) \tag{13}$$

where

$$F(\mathbf{x}^P, \mathbf{x}^Q) = \lim_{\rho_\alpha(\varepsilon)\to 0} \int_{\rho_\alpha(\varepsilon)}^{\rho(P,Q)} \left|J_{\xi\eta}\right| \bar{f}(\mathbf{x}^P, \mathbf{x})/r^\beta(\mathbf{x}^P, \mathbf{x})\rho d\rho \tag{14}$$

in which Q represents the field point which takes on a value from the boundary L as shown in Fig. 2. $\mathbf{n}'(n'_\xi, n'_\eta)$ is the outward normal to the boundary L of the integration boundary. ρ is the local distance defined as $\rho = \sqrt{(\xi-\xi_P)^2 + (\eta-\eta_P)^2}$.

From Fig. 2, it can be seen that

$$\partial\rho(P,Q)/\partial\mathbf{n}' = \rho_{,\xi} n'_\xi + \rho_{,\eta} n'_\eta \tag{15}$$

where

$$\rho_{,\xi} = \left(\xi_Q - \xi_P\right)/\rho(P,Q) = \cos\theta; \qquad \rho_{,\eta} = \left(\eta_Q - \eta_P\right)/\rho(P,Q) = \sin\theta. \tag{16}$$

It is noted that $\rho_{,\xi}$ and $\rho_{,\eta}$ are constant in the radial integral of Eq. (14). Obviously, on the boundary of the integration element, either n'_ξ or n'_η is 0, and the remaining non-zero term is either 1 or -1.

In order to compute the integration, the radial integral of Eq. (14) must be evaluated firstly. For this, the global distance r must be expressed as a power series in the local distance ρ by using Eq. (17)

$$r/\rho = \bar{\rho} = \sum_{n=0}^{N} C_n \rho^n = \sqrt{\sum_{n=0}^{M} G_n \rho^n} \tag{17}$$

where N and M are the orders of the power series, and C_n and G_n are coefficients which can be computed according to [40].

After the G_n and C_n are achieved. Then, substituting Eq. (17) into Eq. (14) yields

$$F(\mathbf{x}^P, \mathbf{x}^Q) = \lim_{\rho_\alpha(\varepsilon)\to 0} \int_{\rho_\alpha(\varepsilon)}^{\rho(P,Q)} \left|J_{\xi\eta}\right| \bar{f}(\mathbf{x}^P, \mathbf{x})/\left(\bar{\rho}^\beta(\rho)\rho^{\beta-1}\right) d\rho. \tag{18}$$

In order to evaluate the singular integral in the above equation, the non-singular part of the integrand is expressed as a power series in the local distance ρ, i.e.

$$\bar{f}(\mathbf{x}^P, \mathbf{x})\left|J_{\xi\eta}\right|/\bar{\rho}^\beta(\rho) = \sum_{k=0}^{K} B_k \rho^k. \tag{19}$$

Following the method in paper [40], the coefficients B_k can be obtained. Then, substituting Eq. (19) into Eq. (18) yields

$$F(\mathbf{x}^P, \mathbf{x}^Q) = \sum_{k=0}^{K} B_k \lim_{\rho_\alpha(\varepsilon)\to 0} \int_{\rho_\alpha(\varepsilon)}^{\rho(Q,P)} \rho^{k-\beta+1} d\rho = \sum_{k=0}^{K} B_k E_k \tag{20}$$

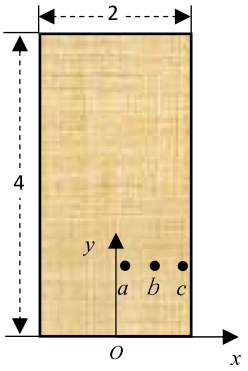

Fig. 3. The isogeometric rectangular surface element.

where

$$E_k = \begin{cases} \left[1/\rho^{\beta-k-2}(Q,P) - \lim\limits_{\rho_\alpha(\varepsilon)\to 0} 1/\rho_\alpha^{\beta-k-2}(\varepsilon)\right] \Big/ (k-\beta+2), & k \neq \beta-2 \\ \ln\rho(Q,P) - \lim\limits_{\rho_\alpha(\varepsilon)\to 0} \ln\rho_\alpha(\varepsilon), & k = \beta-2. \end{cases} \tag{21}$$

After some manipulations (see [37,40,50]), the limiting terms in Eq. (21) can be expressed as summations of finite parts and infinite terms, i.e.

$$\begin{aligned} &\lim_{\rho_\alpha(\varepsilon)\to 0} \ln\rho_\alpha(\varepsilon) = \ln H_0 + \textit{Infinite terms}, \\ &\lim_{\rho_\alpha(\varepsilon)\to 0} 1/\rho_\alpha^{\beta-k-2}(\varepsilon) = H_{\beta-k-2} + \textit{Infinite terms} \end{aligned} \tag{22}$$

where

$$\begin{aligned} &H_0 = 1/C_0; \qquad H_1 = \bar{C}_1; \qquad H_2 = 2\bar{C}_2 - \bar{C}_1^2, \\ &H_3 = 3\bar{C}_3 - 3\bar{C}_1\bar{C}_2 + \bar{C}_1^3, \\ &H_4 = 4\bar{C}_4 + 4\bar{C}_1^2\bar{C}_2 - 4\bar{C}_1\bar{C}_3 - 2\bar{C}_2^2 - \bar{C}_1^4 \end{aligned} \tag{23}$$

in which $\bar{C}_i = C_i/C_0$.

For physical problems, the boundary integrals should exist. Therefore, the infinite terms in Eq. (22) must be eliminated after considering all contributions of adjacent elements around the source point or be canceled out by free terms [51–53]. Thus, substituting Eq. (22) into Eq. (21), it follows that

$$E_k = \begin{cases} \left[1/\rho^{\beta-k-2}(Q,P) - H_{\beta-k-2}\right] \big/ (k-\beta+2), & 0 \le k \le \beta-3 \\ \ln\rho(Q,P) - \ln H_0, & k = \beta-2 \\ \rho^{k-\beta+2}(Q,P) / (k-\beta+2), & k > \beta-2. \end{cases} \tag{24}$$

4. Numerical examples

To illustrate the accuracy and flexibility of 3D IGABEM, several 3D potential examples are now studied in which the proposed method is compared with the analytical solutions.

4.1. Highly singular integrals over isogeometric rectangular surface element

To test our method and program, the following singular integral over a rectangular element (see Fig. 3) with $x \in [-1, 1]$, $y \in [0, 4]$ is considered.

$$I(\boldsymbol{x}^p) = \int_0^4 \int_{-1}^1 \frac{r_{,1}}{r^\beta} dxdy \quad \left(r_{,1} = \frac{\partial r}{\partial x}\right). \tag{25}$$

The problem was analyzed by Gao [40] and his results are also used here as comparison. Three source points (a, b, c) are computed in this example. Table 1 shows the corresponding intrinsic and Cartesian coordinates of the source points in different methods.

Table 1
Corresponding intrinsic (ξ, η) and Cartesian coordinates (x, y, z) of the computed points in two methods.

	Current method		Conventional method [40]	
	(ξ, η)	(x, y, z)	(ξ, η)	(x, y, z)
Point a	(0.75, 0.25)	(0.5,1,0)	(0.5, −0.25)	(0.5,1,0)
Point b	(0.875, 0.25)	(0.75,1,0)	(0.75, −0.5)	(0.75,1,0)
Point c	(0.995, 0.25)	(0.99,1,0)	(0.99, −0.5)	(0.99,1,0)

Table 2
Computed results for various values of β at source points.

	Point a			Point b			Point c		
β	Analytical	Current	Ref. [40]	Analytical	Current	Ref. [40]	Analytical	Current	Ref. [40]
1	−2.057701	−2.0577014	−2.05769	−3.129422	−3.1294224	−3.12942	−4.203354	−4.2033535	−4.20335
2	−1.866635	−1.8666347	−1.86667	−3.42229	−3.4222857	−3.42300	−10.01288	−10.012880	−10.0130
3	−1.947746	−1.9477459	−1.94782	−5.180698	−5.1806975	−5.18065	−156.0485	−156.04847	−156.048
4	−2.293076	−2.2930759	−2.29308	−10.34099	−10.340986	−10.3410	−6666.374	−6666.3736	−6666.37
5	−2.980266	−2.9802663	−2.980264	−24.99558	−24.995577	−24.99557	−392699.0	−392698.96	−392698.9
6	−4.186087	−4.1860870	−4.18575	−68.19732	−68.197317	−68.19818	-2.667×10^7	-2.6666667×10^7	-2.667×10^7

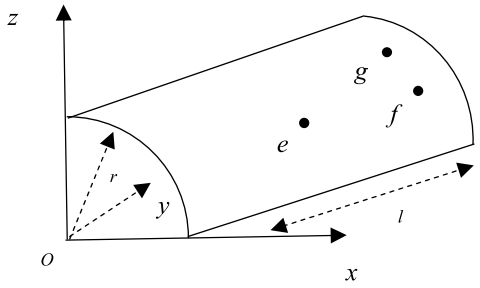

Fig. 4. 3D isogeometric cylindrical surface element.

Table 2 lists the computed results for singularity orders of β from 1 to 6. Results in [40] and analytical results are also listed in Table 2. From Table 2, it can be seen that the current results are in excellent agreement with the analytical results. The results in [40] are also acceptable, which means both the NURBS interpolation and conventional interpolation method are effective for rectangular surface element. In fact, with the shape of integration element becoming more and more complex, the advantage of the present method will be more obvious, which can be seen in the following examples.

When the contour integral shown in Eq. (14) is computed, we also used the subdivision technique [38,54]. Thus, even if the source point is very close to the boundary of the element (the minimum distance to the boundary is 0.01), good results can still be achieved.

4.2. Highly singular integral over isogeometric cylindrical surface element

In this example, we consider the following hypersingular integral (see Eq. (26)) over a 3D isogeometric cylindrical surface element. The surface element is a 90° cylindrical panel with $r = 1$, $l = 2$, as shown in Fig. 4. The corresponding polynomial orders and knot vectors are given in Table 3.

$$I(x^p) = -\frac{1}{4\pi}\int_S \frac{1}{r^3}\left(3r_{,3}\frac{\partial r}{\partial n} - n_3\right) dS. \tag{26}$$

This problem has been analyzed by Guiggiani et al. [37] and Gao [40] and their results are used here as comparison. Table 4 gives the intrinsic and Cartesian coordinates of the computed points in different methods. The distance between the computed points to the center of the cylinder are also given in Table 4, which tells us that both points e and f are on the real boundary of the element for current and conventional methods. But, for conventional method the point g is not on the real boundary, because the distance $d(d = \sqrt{x^2 + z^2})$ to the center of the cylinder is less than $r = 1.0$, which may arise as big error in numerical computation. In contrast, for the current method the point g is on the real boundary (distance is equal to $r = 1.0$).

Table 5 gives the computed results for points e, f and g, respectively. From Table 5, it can be seen that the absolute values of current results are a little bigger than those in [37,40]. The reason is that the integration of current method is computed on the real boundary rather than the approximated boundary. Thus, the current results are more accurate. However, as shown in Table 4 the source point g in [37,40] is not on the real boundary, so larger error appears. To examine the dependence of

Table 3
Polynomial orders and knot vectors for the isogeometric boundary element.

Direction	Order	Knot vector
ξ	$p = 2$	$\mathbf{U} = \{0, 0, 0, 1, 1, 1\}$
η	$q = 2$	$\mathbf{V} = \{0, 0, 0, 1, 1, 1\}$

Table 4
The intrinsic (ξ, η) and Cartesian coordinates (x, y, z) of the computed points in different methods.

	Current method			Conventional method [40]		
	(ξ, η)	(x, y, z)	d	(ξ, η)	(x, y, z)	d
Point e	(0.5,0.5)	$(\sqrt{2}/2, 1, \sqrt{2}/2)$	1.0	(0,0)	$(\sqrt{2}/2, 1, \sqrt{2}/2)$	1.0
Point f	(0.83,0.5)	$(\sqrt{2}/2, 1.66, \sqrt{2}/2)$	1.0	(0.66,0)	$(\sqrt{2}/2, 1.66, \sqrt{2}/2)$	1.0
Point g	(0.83,0.83)	(0.24902888, 1.66, 0.96849606)	1.0	(0.66,0.66)	(0.28689107,1.66, 0.94689107)	0.9894

Table 5
Computed results for the source points.

	Point e	Point f	Point g
Ref. [37]	−0.343918	−0.497119	−0.876365
Ref. [40]	−0.343918	−0.497108	−0.876377
Current	−0.34401438	−0.49801601	−0.96352894

Table 6
Parametric study for varying numbers of Gauss points.

Number of Gauss points	Point e	Point f	Point g
4	−3.4511321E−01	−4.5718893E−01	−8.1780331E−01
10	−3.4401551E−01	−4.9760480E−01	−9.6413261E−01
16	−3.4401438E−01	−4.9801296E−01	−9.6360642E−01
24	−3.4401438E−01	−4.9801601E−01	−9.6352907E−01
30	−3.4401438E−01	−4.9801601E−01	−9.6352895E−01
34	−3.4401438E−01	−4.9801601E−01	−9.6352894E−01
36	−3.4401438E−01	−4.9801601E−01	−9.6352894E−01

Table 7
Computed results for the source points.

Points	Cartesian coordinates (x, y, z)	Intrinsic coordinates (ξ, η)	Exact	Current
h	(20, 0, 0)	(0, 0)	1.8760262	1.8760259
i	(14.1421356, 14.1421356, 0)	(0.5, 0)	2.8988373	2.8988374
j	(18.5355339, 0, 3.5355339)	(0, 0.5)	2.3224465	2.3224464
k	(13.1066017, 13.1066017, 3.5355339)	(0.5, 0.5)	3.7439683	3.7439683

the computational results on the number of Gauss points, parametric study for varying numbers of Gauss points has been performed and the results are listed in Table 6. It is easy to see that the results are stable and good convergence can be achieved.

4.3. A representative singular integral of 3D potential problems

$$I(x^p) = \int_S 1/(4\pi r)\, dS. \tag{27}$$

This example is concerned with the following surface integral (see Eq. (27)) over a curved 3D isogeometric boundary element. This integral is representative of the singular integrals in the potential problems. The surface element is part of a ring surface as shown in Fig. 5. It is represented with only one element and the corresponding polynomial orders will be $p = q = 2$, respectively. The element is defined by two knot vectors $\mathbf{U} = \{0, 0, 0, 1, 1, 1\}$ and $\mathbf{V} = \{0, 0, 0, 1, 1, 1\}$.

Four source points h, i, j and k are computed corresponding to intrinsic coordinates (0,0), (0,0.5), (0.5,0) and (0.5,0.5), respectively. Table 7 lists the computed results. Since the integrals described above are not amenable to analytic integration, 'exact' values for these integrals are found using the subdivision method. From Table 7, it can also be seen that the current results are in good agreement with the exact results, even for the source point being on the boundary of the element ($\xi = 0$ or $\eta = 0$).

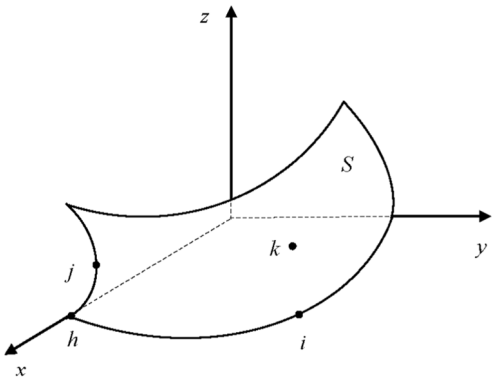

Fig. 5. 3D isogeometric ring surface element.

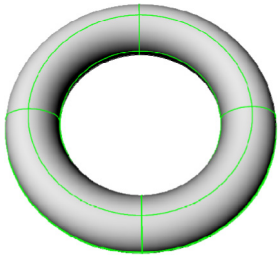

Fig. 6. The isogeometric model of ring surface.

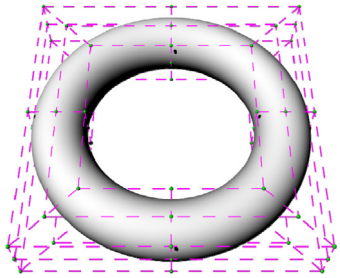

Fig. 7. The control points of the ring surface.

Table 8
Polynomial orders and knot vectors for the isogeometric boundary element.

Direction	Order	Knot vector
ξ	$p = 2$	$\mathbf{U} = \{0, 0, 0, 1, 1, 2, 2, 3, 3, 4, 4, 4\}$
η	$q = 2$	$\mathbf{V} = \{0, 0, 0, 1, 1, 2, 2, 3, 3, 4, 4, 4\}$

4.4. Potential problem for a 3D ring

A 3D ring surface is used for discussion, which is shown in Fig. 6. To describe this model the corresponding polynomial orders and knot vectors are given in Table 8. The control points are displayed in Fig. 7. The potential on the boundary is given as $u = x + 3y/4 + 7z/5 + 9/5$.

Table 9 shows the numerical results of potential when the computed points are moving along the following curve (S1) and the exact solutions are given as comparison.

$$\text{S1} : x = R\cos\theta,\ \ y = R\sin\theta,\ \ z = 0 \tag{28}$$

where $R = 15$. From Table 9, we can clearly see that the current solutions are in good agreement with the exact results. In addition, 64 boundary points on the surface of the model are taken into account. Fig. 8(a) and (b) display the profiles of the exact and current solutions for the flux q $(= \partial u/\partial \mathbf{n})$, respectively. Hence, we can see from Fig. 8(a) and (b) that the numerical results match the exact solution very well. Fig. 9 shows the relative error surfaces of the computational results for the flux at 64 points. It can be seen that the proposed method is accurate. Here one should note that an average relative

Table 9
The numerical results of potential at the interior points.

Point	θ	Exact solution	Current solution	Error
1	0	0.1679988E+02	0.1680000E+02	0.7423874E−05
2	$\pi/4$	0.2036154E+02	0.2036155E+02	0.8006295E−06
3	$\pi/2$	0.1304991E+02	0.1305000E+02	0.7167879E−05
4	$3\pi/4$	−0.8516481E+00	−0.8516504E+00	0.2726892E−05
5	π	−0.1319988E+02	−0.1320000E+02	0.9448567E−05
6	$5\pi/4$	−0.1676154E+02	−0.1676155E+02	0.9719072E−06
7	$3\pi/2$	−0.9449906E+01	−0.9450000E+01	0.9898499E−05
8	$7\pi/4$	0.4451648E+01	0.4451650E+01	0.5242428E−06

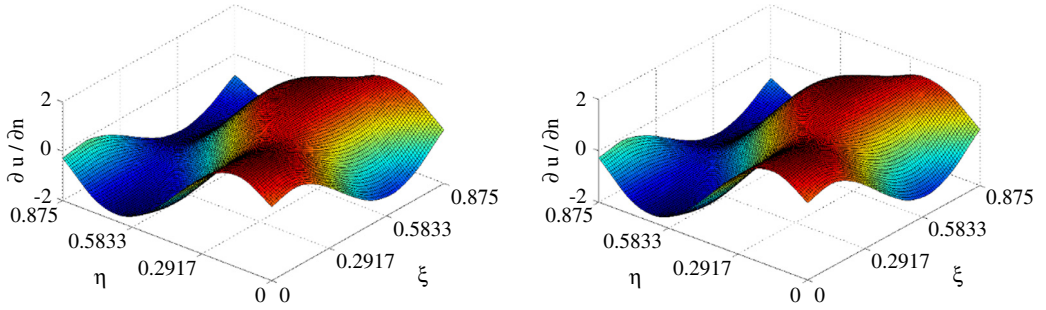

(a) Analytical solutions. (b) Numerical solutions.

Fig. 8. Profiles of solutions for the potentials.

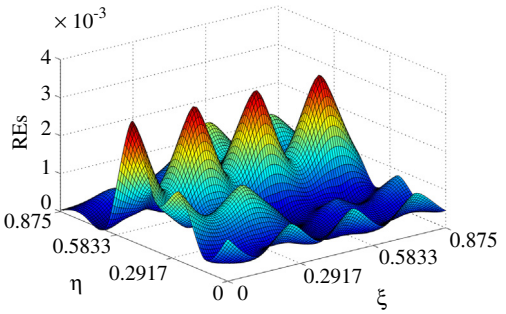

Fig. 9. Surface of REs for the flux.

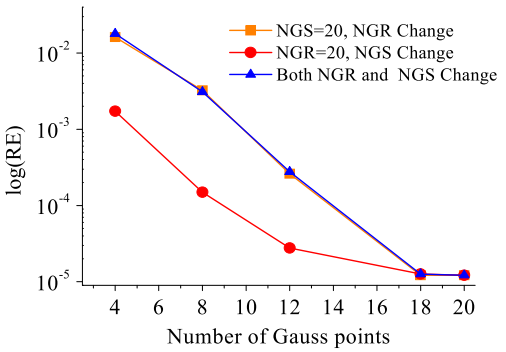

Fig. 10. Convergence curves of potential at interior point with different Gaussian points.

error (RE) is given as $\left|I^k_{num} - I^k_{exact}\right| / \left|I^k_{exact}\right|$ (I^k_{num} and I^k_{exact} denote the numerical and analytical solutions at the kth point, respectively.) which is also used in the following examples.

To study the influence of the number of the Gauss points, Fig. 10 gives the relative errors of point with $\theta = 5\pi/8$ and $R = 15$. In Fig. 10, NGR and NGS represent the numbers of Gauss points for regular and singular integrals, respectively. We can observe that the convergence rates are rapid with the increase of the number of Gauss points.

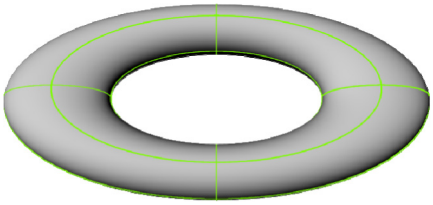

Fig. 11. The model of ellipse surface.

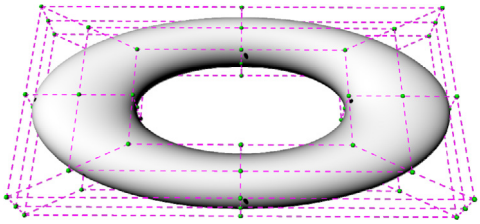

Fig. 12. The control points of the ellipse surface.

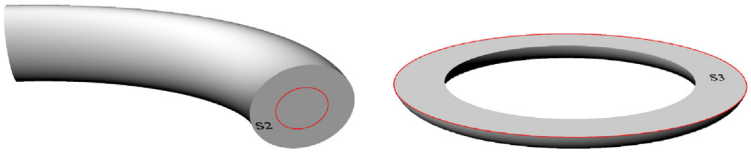

(a) Points inside the surface. (b) Points on the surface.

Fig. 13. The computed points along the curves (a) S2 and (b) S3.

4.5. Potential problem for a 3D Ellipse surface.

In this case, an ellipse surface as shown in Fig. 11 is used for analysis, which is modeled by Rhinoceros. For this model, the knot vectors are the same as Table 8. The control points are displayed in Fig. 12. The Dirichlet boundary conditions corresponding to the exact solution (Eq. (29)) are imposed on the ellipse surface.

$$u = 10x - 25y/18 + 11z/5. \tag{29}$$

In order to study the convergence rate, two sets of nodes, i.e. (a) 64 and (b) 256, have been used for discretization of the body surface. The potential u inside the model along the following curve (Fig. 13(a)) is considered.

$$\mathrm{S2} : x = r\cos\theta, y = 0, z = r\sin\theta \tag{30}$$

where $r = 2$. Fig. 14 shows that the numerical results are in good agreement with the exact solution, even for the calculation from 64 nodes. In addition, the relative errors of normal flux q on the surface labeled by red curve (S3) with parameter coordinate (ξ, $\eta = 0$) are given in Fig. 13(b). Fig. 15 shows the relative errors of numerical results of flux q on surface points along the red curve S3, from which it can be seen that the REs decrease significantly with the increment of nodes on the body surface. This numerical example testifies again that the present method is effective to solve the potential problems.

4.6. Potential problem for a 3D complex surface

Finally, to illustrate the ability of present method to handle arbitrary geometries which can be taken directly from CAD, a problem with complex surface as shown in Fig. 16 is analyzed. The physical quantities on the boundary surface are given as $u = 11x + 7y/4 + 5z - 3$.

There are two sets of nodes, i.e. (a) 192 nodes and (b) 768 nodes, which are used for discretization of the body surfaces. The quadratic bivariate NURBS are applied for approximation of boundary variables. In order to test our method, the potential of points inside the surface labeled by red curves (S4, S5) in Fig. 17 is considered. The relative errors of the computed points are given in Fig. 18(a) and (b), from which we can see that the relative errors of the computed point are very small. Fig. 18(a) and (b) also show that the numerical results are convergent with the increment of nodes on the body surfaces.

Furthermore, the normal flux q of points on the surface labeled by red curve (S6) is also considered. Fig. 19 gives the numerical results of q along the curve S6. It is easy to see that the numerical results obtained from quadratic NURBS approximation are convergent to the exact solutions with the increase of nodes on the body surfaces. Moreover, the relative

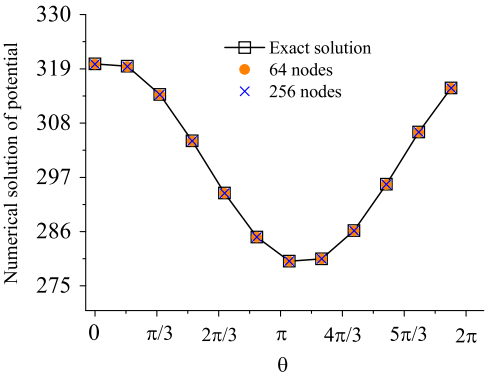

Fig. 14. The numerical results of potential along S2.

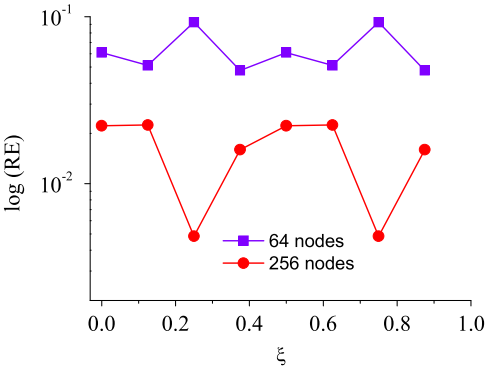

Fig. 15. The relative errors of flux along the S3.

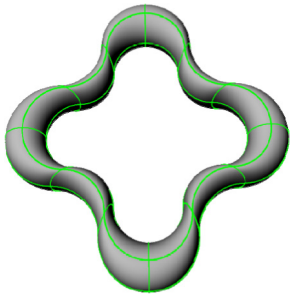

Fig. 16. The model of 3D complex surface.

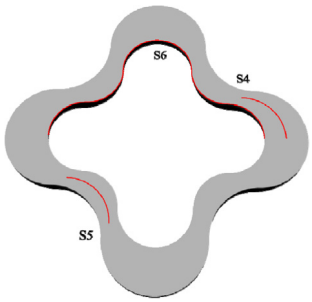

Fig. 17. The points considered in this example.

errors of the numerical results are given in Fig. 20, from which we can observe that the convergence rates are fast with the increase of nodes on the body surfaces.

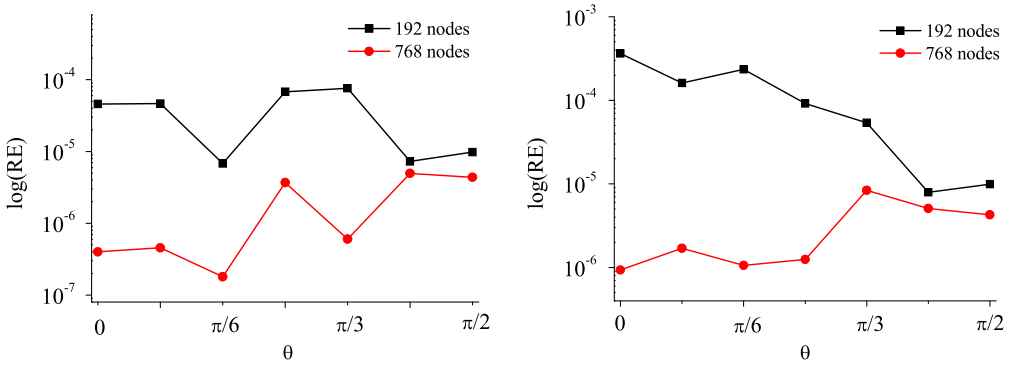

(a) Points along the curve S4.

(b) Points along the curve S5.

Fig. 18. The relative errors of potential.

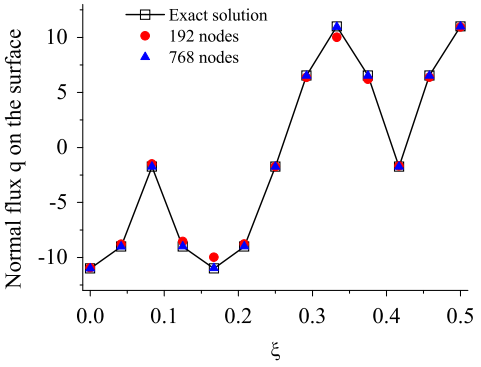

Fig. 19. Variation of normal flux along the line S6.

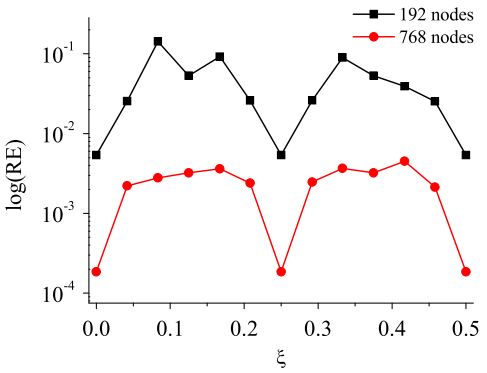

Fig. 20. The relative errors of flux along the line S6.

This example shows that it is possible to integrate CAD and 3D IGABEM into a really seamless design/analysis. In present method only knot vectors, control points and the corresponding weights are needed to define the mesh and all of them can be easily obtained by CAD. Therefore, it is possible to analyze practical problems whose geometries must be described by NURBS using the present method.

5. Conclusions

In this paper, 3D IGABEM for potential problems has been presented. The geometry of the 3D model and the approximation spaces for the physical quantities are all provided, using the isoparametric concept, from a set of NURBS basis functions. To accurately evaluate the singular integrals appearing in our method, the power series expansion method is employed, in which the non-singular part of a singular integrand as well as the global distance r is expressed as power series in the local distance ρ of the intrinsic coordinate system. In contrast to the original power series expansion method,

one of the features of the present method is that the integration surface is on the real surface of the model, rather than the interpolation surface, i.e. no geometrical errors. Thus, the value of integral is more accurate than the traditional boundary element method.

The present method offers distinct advantage over conventional 3D BEM, which used the piecewise polynomial formulations. Firstly, the models for analysis in the present method are exact geometrical representation no matter how coarse the discretization of the studied bodies is, it ensures that no geometrical errors exist in the analysis process. Secondly, a meshing process is no longer required because the control points defining the body play the role of nodes in the 3D IGABEM analysis.

Acknowledgment

The research is supported by the National Natural Science Foundation of China (11132011, 11272054, 11672038).

References

[1] T.J.R. Hughes, J.A. Cottrell, Y. Bazilevs, Isogeometric analysis: CAD, finite elements, NURBS, exact geometry and mesh refinement, Comput. Methods Appl. Mech. Engrg. 194 (2005) 4135–4195.
[2] G. Farin, J. Hoschek, M.-S. Kim (Eds.), Handbook of Computer Aided Geometric Design, Elsevier, Amsterdam, 2002.
[3] C. Politis, A.I. Ginnis, P.D. Kaklis, K. Belibassakis, C. Feurer, An isogeometric BEM for exterior potential-flow problems in the plane, in: 2009 SIAM/ACM. Proceedings of the Joint Conference on Geometric and Physical Modeling, SPM'09, 2009, pp. 349–354.
[4] K. Li, X. Qian, Isogeometric analysis and shape optimization via boundary integral, Comput. Aided Des. 43 (2011) 1427–1437.
[5] R.N. Simpson, S.P.A. Bordas, J. Trevelyan, T. Rabczuk, A two-dimensional isogeometric boundary element method for elastostatic analysis, Comput. Methods Appl. Mech. Engrg. 209–212 (2012) 87–100.
[6] R.N. Simpson, S.P.A. Bordas, H. Lian, J. Trevelyan, An isogeometric boundary element method for elastostatic analysis: 2D implementation aspects, Comput. Struct. 118 (2013) 2–12.
[7] Y. Bai, C.Y. Dong, Z.Y. Liu, Effective elastic properties and stress states of doubly periodic array of inclusions with complex shapes by isogeometric boundary element method, Compos. Struct. 128 (2015) 54–69.
[8] J.L. Gu, J.M. Zhang, L.F. Chen, Z.H. Cai, An isogeometric BEM using PB-spline for 3-D linear elasticity problem, Eng. Anal. Bound. Elem. 56 (2015) 154–161.
[9] A. Aimi, M. Diligenti, M.L. Sampoli, A. Sestini, Isogemetric analysis and symmetric Galerkin BEM: A 2D numerical study, Appl. Math. Comput. 272 (2016) 173–186.
[10] T. Takahashi, T. Matsumoto, An application of fast multipole method to isogeometric boundary element method for Laplace equation in two dimensions, Eng. Anal. Bound. Elem. 36 (2012) 1766–1775.
[11] R.N. Simpson, Z. Liu, Acceleration of isogeometric boundary element analysis through a black-box fast multipole method, Eng. Anal. Bound. Elem. 66 (2016) 168–182.
[12] M.J. Peake, J. Trevelyan, G. Coates, Extended isogeometric boundary element method (XIBEM) for two-dimensional Helmholtz problems, Comput. Methods Appl. Mech. Engrg. 259 (2013) 93–102.
[13] K.A. Belibassakis, Th.P. Gerostathis, K.V. Kostas, C.G. Politis, P.D. Kaklis, A.I. Ginnis, C. Feurer, A BEM-isogeometric method for the ship wave-resistance problem, Ocean Eng. 60 (2013) 53–67.
[14] A.I. Ginnisa, K.V. Kostasb, C.G. Politisb, P.D. Kaklisa, K.A. Belibassakisa, Th.P. Gerostathisb, M.A. Scottd, T.J.R. Hughes, Isogeometric boundary-element analysis for the wave-resistance problem using T-splines, Comput. Methods Appl. Mech. Engrg. 279 (2014) 425–439.
[15] R.N. Simpson, M.A. Scott, M. Taus, D.C. Thomas, H. Lian, Acoustic isogeometric boundary element analysis, Comput. Methods Appl. Mech. Engrg. 269 (2014) 265–290.
[16] M.J. Peake, J. Trevelyan, G. Coates, Extended isogeometric boundary element method (XIBEM) for three-dimensional medium-wave acoustic scattering problems, Comput. Methods Appl. Mech. Engrg. 284 (2015) 762–780.
[17] K.V. Kostas, A.I. Ginnis, C.G. Politis, P.D. Kaklis, Ship-hull shape optimization with a T-spline based BEM–isogeometric solver, Comput. Methods Appl. Mech. Engrg. 284 (2015) 611–622.
[18] E. Gillebaart, R. De Breuker, Low-fidelity 2D isogeometric aeroelastic analysis and optimization method with application to a morphing airfoil, Comput. Methods Appl. Mech. Engrg. 305 (2016) 512–536.
[19] Minho Yoon, Seonho Cho, Isogeometric shape design sensitivity analysis of elasticity problems using boundary integral equations, Eng. Anal. Bound. Elem. 66 (2016) 119–128.
[20] Y.J. Wang, D.J. Benson, Multi-patch nonsingular isogeometric boundary element analysis in 3D, Comput. Methods Appl. Mech. Engrg. 293 (2015) 71–91.
[21] M. Feischl, G. Gantner, D. Praetorius, Reliable and efficient a posteriori error estimation for adaptive IGA boundary element methods for weakly-singular integral equations, Comput. Methods Appl. Mech. Engrg. 290 (2015) 362–386.
[22] B.H. Nguyen, H.D. Tran, C. Anitescu, X. Zhuang, T. Rabczuk, An isogeometric symmetric Galerkin boundary element method for two-dimensional crack problems, Comput. Methods Appl. Mech. Engrg. 306 (2016) 252–275.
[23] M. Feischl, G. Gantner, A. Haberl, D. Praetorius, Adaptive 2D IGA boundary element methods, Eng. Anal. Bound. Elem. 62 (2016) 141–153.
[24] W. John, T.K. Tsay, Analytical evaluation and application of the singularities in boundary element method, Eng. Anal. Bound. Elem. 29 (2005) 241–256.
[25] G.S. Padhi, R.A. Shenoi, S.S.J. Moy, et al., Analytical Integration of kernel shape function product integral in the boundary element method, Comput. Struct. 79 (2001) 1325–1333.
[26] M.A. Lifeng, A.M. Korsunsky, A note on the Gauss-Jacobi quadrature formulae for singular integral equations of the second kind, Int. J. Fract. 126 (2004) 339–405.
[27] O. Huber, A. Lang, G. Kuhn, Evaluation of the stress tensor in 3D elastostatics by direct solving of hyper singular integrals, Comput. Mech. 12 (1993) 39–50.
[28] G. Karami, D. Derakhshan, An efficient method to evaluate hyper singular and super singular integrals in boundary integral equations analysis, Eng. Anal. Bound. Elem. 23 (1999) 317–326.
[29] J.C.F. Telles, A self-adaptive coordinate transformation for efficient numerical evaluation of general boundary element integrals, Internat. J. Numer. Methods Engrg. 24 (1987) 959–973.
[30] M. Cerrolaza, E. Alarcón, A bi-cubic transformation for the numerical evaluation of the Cauchy principal value integrals in boundary methods, Internat. J. Numer. Methods Engrg. 28 (1989) 987–999.
[31] Z.R. Niu, H.L. Zhou, A novel boundary integral equation method for linear elasticity-natural boundary integral equation, Acta Mech. Solida Sin. 14 (2001) 1–10.
[32] H.R. Kutt, The numerical evaluation of principal value integrals by finite-part integration, Numer. Math. 24 (1975) 205–210.
[33] H.R. Kutt, Quadrature formulae for finite-part integrals, in: Technical Report CSIR Special Report WISK 178, National Research Institute for Mathematical Sciences, CSIR, South Africa, 1975.

[34] J. Dominguez, M.P. Ariza, R. Gallego, Flux and traction boundary elements without hyper singular or strongly singular integrals, Internat. J. Numer. Methods Engrg. 48 (2000) 111–135.
[35] A.B. Jorge, G.O. Ribeiro, T.A. Cruse, et al., Self-regular boundary integral equation formulations for Laplace's equation in 2-D, Internat. J. Numer. Methods Engrg. 51 (2001) 1–29.
[36] M. Guiggiani, P. Casalini, Direct computation of Cauchy principal value integrals in advanced boundary elements, Internat. J. Numer. Methods Engrg. 24 (1987) 1711–1720.
[37] M. Guiggiani, G. Krishnasamy, T.J. Rudolphi, et al., General algorithm for the numerical solution of hyper-singular boundary integral equations, J. Appl. Mech. 59 (1992) 604–614.
[38] X.W. Gao, K. Yang, J. Wang, An adaptive element subdivision technique for evaluation of various 2D singular boundary integrals, Eng. Anal. Bound. Elem. 32 (2008) 692–696.
[39] X.W. Gao, Numerical evaluation of two-dimensional singular boundary integrals-Theory and Fortran code, J. Comput. Appl. Math. 188 (2006) 44–64.
[40] X.W. Gao, An effective method for numerical evaluation of general 2D and 3D high order singular boundary integrals, Comput. Methods Appl. Mech. Engrg. 199 (2010) 2856–2864.
[41] X.W. Gao, The radial integration method for evaluation of domain integrals with boundary-only discretization, Eng. Anal. Bound. Elem. 26 (2002) 905–916.
[42] X.W. Gao, A boundary element method without internal cells for two-dimensional and three-dimensional elastoplastic problems, J. Appl. Mech. 69 (2002) 154–160.
[43] V.P. Nguyen, T. Rabczuk, S. Bordas, et al., Meshless methods: A review and computer implementation aspects, Math. Comput. Simulation 79 (2008) 763–813.
[44] G.Z. Xie, F.L. Zhou, J.M. Zhang, et al., New variable transformations for evaluating nearly singular integrals in 3D boundary element method, Eng. Anal. Bound. Elem. 37 (2013) 1169–1178.
[45] K. Hayami, H. Matsumoto, A numerical quadrature for nearly singular boundary element integrals, Eng. Anal. Bound. Elem. 13 (1994) 143–154.
[46] J.H. lv, Y. Miao, H.P. Zhu, The distance sinh transformation for the numerical evaluation of nearly singular integrals over curved surface elements, Comput. Mech. 53 (2014) 359–369.
[47] F.J. Wang, W. Chen, W.Z. Qu, Y. Gu, A BEM formulation in conjunction with parametric equation approach for three-dimensional inverse heat conduction problems, Eng. Anal. Bound. Elem. 63 (2016) 1–14.
[48] T.N.E. Greville, Numerical procedures for interpolation by spline functions, Mon. Not. R. Astron. Soc. 1 (1964) 53–68.
[49] R.W. Johnson, Higher order B-spline collocation at the Greville abscissae, Appl. Numer. Math. 52 (2005) 63–75.
[50] G. Karami, D. Derakhshan, G. Karami, et al., An efficient method to evaluate hypersingular and supersingular integrals in boundary integral equations analysis, Eng. Anal. Bound. Elem. 23 (1999) 317–326.
[51] A. Frangi, M. Guiggiani, A direct approach for boundary integral equations with high-order singularities, Internat. J. Numer. Methods Engrg. 49 (2000) 871–898.
[52] M. Bonnet, M. Guiggiani, Direct evaluation of double singular integrals and new free terms in 2D (symmetric) Galerkin BEM, Comput. Methods Appl. Mech. Engrg. 192 (2003) 2565–2596.
[53] A. Frangi, M. Guiggiani, Free terms and compatibility conditions for 3D hypersingular boundary integral equations, ZAMM. J. Appl. Math. Mech. 81 (2001) 651–664.
[54] X.W. Gao, T.G. Davies, Boundary Element Programming in Mechanics, Cambridge University Press, 2011.